A study of planar Richtmyer-Meshkov instability in fluids with Mie-Grüneisen equations of state

G. M. Ward[a] and D. I. Pullin[b]
Graduate Aeronautics Laboratory at the California Institute of Technology, MC 205-45, Pasadena, California 91125, USA

(Received 28 June 2010; accepted 23 May 2011; published online 15 July 2011)

We present a numerical comparison study of planar Richtmyer-Meshkov instability with the intention of exposing the role of the equation of state. Results for Richtmyer-Meshkov instability in fluids with Mie-Grüneisen equations of state derived from a linear shock-particle speed Hugoniot relationship (Jeanloz, J. Geophys. Res. **94**, 5873, 1989; McQueen *et al.*, *High Velocity Impact Phenomena* (1970), pp. 294–417; Menikoff and Plohr, Rev. Mod. Phys. **61**(1), 75 1989) are compared to those from perfect gases under nondimensionally matched initial conditions at room temperature and pressure. The study was performed using Caltech's Adaptive Mesh Refinement, Object-oriented C++ (AMROC) (Deiterding, Adaptive Mesh Refinement: Theory and Applications (2005), Vol. 41, pp. 361–372; Deiterding, "Parallel adaptive simulation of multi-dimensional detonation structures," Ph.D. thesis (Brandenburgische Technische Universität Cottbus, September 2003)) framework with a low-dissipation, hybrid, center-difference, limiter patch solver (Ward and Pullin, J. Comput. Phys. **229**, 2999 (2010)). Results for single and triple mode planar Richtmyer-Meshkov instability when a reflected shock wave occurs are first examined for mid-ocean ridge basalt (MORB) and molybdenum modeled by Mie-Grüneisen equations of state. The single mode case is examined for incident shock Mach numbers of 1.5 and 2.5. The planar triple mode case is studied using a single incident Mach number of 2.5 with initial corrugation wavenumbers related by $k_1 = k_2 + k_3$. Comparison is then drawn to Richtmyer-Meshkov instability in perfect gases with matched nondimensional pressure jump across the incident shock, post-shock Atwood ratio, post-shock amplitude-to-wavelength ratio, and time nondimensionalized by Richtmyer's linear growth time constant prediction. Differences in start-up time and growth rate oscillations are observed across equations of state. Growth rate oscillation frequency is seen to correlate directly to the oscillation frequency for the transmitted and reflected shocks. For the single mode cases, further comparison is given for vorticity distribution and corrugation centerline shortly after shock interaction. Additionally, we examine single mode Richtmyer-Meshkov instability when a reflected expansion wave is present for incident Mach numbers of 1.5 and 2.5. Comparison to perfect gas solutions in such cases yields a higher degree of similarity in start-up time and growth rate oscillations. The formation of incipient weak waves in the heavy fluid driven by waves emanating from the perturbed transmitted shock is observed when an expansion wave is reflected. © *2011 American Institute of Physics*. [doi:10.1063/1.3607444]

I. INTRODUCTION

The impulsive acceleration of a corrugated material contact by shock wave is one of the most fundamental research topics in the area of compressible flows. Applications for such research are numerous and vast in complexity, ranging from supernovas to inertial confinement fusion (ICF) to hypervelocity impacts in solids. Richtmyer[7] and Meshkov[8] were first to draw attention to the topic, proposing a simple incompressible model that leads to a linear growth prediction for the corrugation amplitude. A great deal of research has been performed on Richtmyer-Meshkov instability since its introduction.[9–23] A common component of most previously performed experimental and computational work has been the use of gases at conditions close to room temperature and pressure. In light of this, the current investigation is focused on exploring the role of the equation of state in Richtmyer-Meshkov instability specifically in relation to commonly studied perfect gas cases. To achieve this goal, we present a numerical comparison study between planar Richtmyer-Meshkov instability in fluids with Mie-Grüneisen equation of state derived from shock Hugoniots of solids and perfect gases initially at room temperature and pressure.

The majority of prior numerical studies of Richtmyer-Meshkov instability have focused on the perfect gas equation of state, often with a single gamma, owing to challenges associated with the numerical modeling of multiphase flows.[24] Presently, we utilize a solver that was developed to address such numerical challenges created by Mie-Grüneisen equation of state.[6] The solver combines a low dissipation, skew-symmetric, kinetic-energy preserving, and center-difference method with a Roe-Riemann solver to provide efficient treatment of smooth and sharp flow features. To avoid ill-posed vortex sheets associated with truly discontinuous interfaces,[25] we use a fluid-mixture like approach for multiphase Mie-Grüneisen flows.

[a]Electronic mail: geoff@caltech.edu.
[b]Electronic mail: dale@galcit.caltech.edu. URL: http://fluids.caltech.edu/.

 © 2011 American Institute of Physics

Downloaded 02 Sep 2011 to 131.215.220.186. Redistribution subject to AIP license or copyright; see http://pof.aip.org/about/rights_and_permissions

Catastrophic numerical oscillations that occur in such mixed phased treatments are eliminated by tracking additional density dependent functions associated with the equation of state.[26] The solver is implemented as a patch solver in Caltech's virtual test facility (VTF) software suite with object-oriented C++ adaptive mesh refinement (AMROC).[4,5,27]

Two distinct variations of Richtmyer-Meshkov instability are commonly noted. The first, more commonly studied, involves a shock wave that begins in a lighter fluid and travels until it reaches a corrugated heavier fluid. Upon reaching the material contact, misaligned gradients of thermodynamic quantities results in baroclinic deposition of vorticity, leading to the growth of corrugation amplitude. Transmitted and reflected shock waves move away from the now growing corrugation. This situation, often denoted as "light-to-heavy" Richtmyer-Meshkov instability, is schematically depicted in Figure 1(a). To the right of the schematic, Figure 1(b), is a wave diagram for the related zero-corrugation Riemann problem showing the position of the shocks and material contact as a function of time. The frame of reference, as is the case for all simulations presented here, is such that the interface is stationary post-shock for zero-corrugation amplitude. Figure 2(a) depicts the second case of interest in which a reflected expansion wave occurs instead of a shock. To achieve the reflected expansion wave, the shock must start out in the heavy fluid. Although a reflected shock can occur sometimes, the situation is generally referred to as "heavy-to-light" Richtmyer-Meshkov instability. For such cases, a phase reversal for the corrugation is also observed due to the difference in the direction of the density gradient yielding baroclinic vorticity generation opposite in sign to that of the "light-to-heavy" case. The wave diagram for the associated zero-corrugation problem is depicted in Figure 2(b). Due to the difference in the reflected wave created by the shock-corrugation interaction in the above discussed situations, variation in the solution is expected.

In attempting to make comparison between flows with different equations of state, it is useful to try to define some level of flow similarity. A variety of theoretical and experimental work has been performed on Richtmyer-Meshkov instability that yields insight into what would be required to achieve a high level of similarity. From simple consideration of the associated one-dimensional Riemann problem, it is clear that a set of nondimensional parameters involving corrugation wavenumber, shock speeds, speeds of sound, densities, shock Hugoniot slopes, and incident shock strength are important for achieving similarity in the case of a small corrugation. It is impossible to match all of the quantities in any such nondimensional set for flows with vastly different equations of state. This is the underlying reason for our present study and comparison. As a starting point, we match several key parameters between flows in spite of the impossibility of achieving full similarity. The choice of these parameters is somewhat arbitrary in nature but provides a useful basis for comparison. We match the post-shock Atwood ratio, a nondimensional pressure ratio across the incident shock, the ratio of post-shock corrugation amplitude-to-wavelength ratio, and time nondimensionalized by the Richtmyer growth prediction time constant. A parameter study of two arbitrary Mach numbers of 1.5 and 2.5 in fluids with Mie-Grüneisen equations of state forms a basis for comparison of single mode instability. A matching set of initial conditions for perfect gas flows is generated based on these two cases.

For the purposes of the present investigation, we begin in Sec. VI by studying two incident shock Mach numbers, 1.5 and 2.5 for the "light-to-heavy" case with a single mode corrugation in fluids with Mie-Grüneisen equation of state. For comparison purposes, we also examine the equivalent matched perfect gas cases. For both equations of state, amplitude and growth rate results are examined in detail in Subsection VI followed by integral vorticity in Subsection VI C and corrugation centerline shortly post-shock in Subsection VI D. Comparison to prediction for the evolution of the bubble position in the nonlinear regime is then examined in Subsection VI B. For a single incident Mach number of 2.5, in Sec. VII, we next examine a triple mode case of three corrugation wave numbers with the property that $k_1 = k_2 + k_3$ and $k_1 h_1 = k_2 h_2 = k_3 h_3$. Instability amplitude and growth rate are again examined for both equations of state in Subsection VII A. Lastly, in Sec. VIII, we study single mode "heavy-to-light" Richtmyer-Meshkov instability, again utilizing two

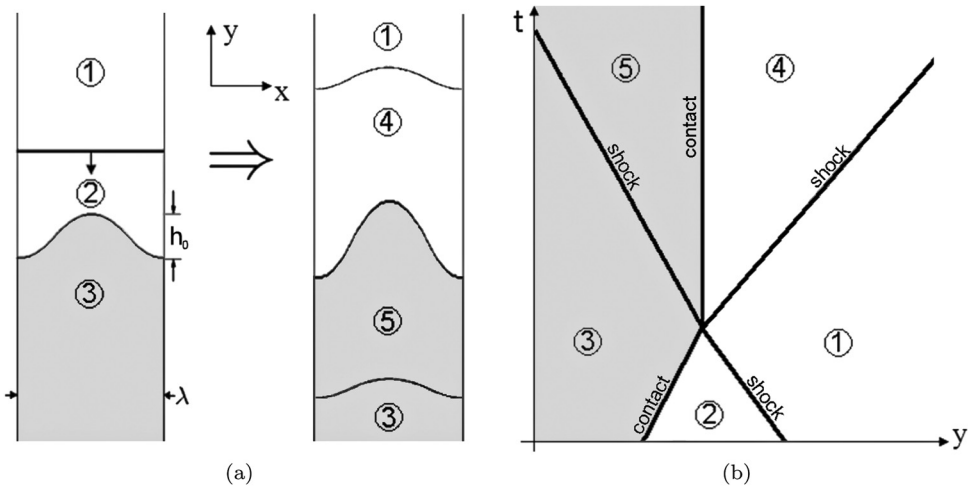

(a) (b)

FIG. 1. (a) Schematic depiction of Richtmyer-Meshkov instability for the case in which the shock starts in the light fluid, resulting in perturbed reflected and transmitted shock waves. (b) Schematic depiction of the *y-t* diagram for the associated one-dimensional Riemann problem.

Downloaded 02 Sep 2011 to 131.215.220.186. Redistribution subject to AIP license or copyright; see http://pof.aip.org/about/rights_and_permissions

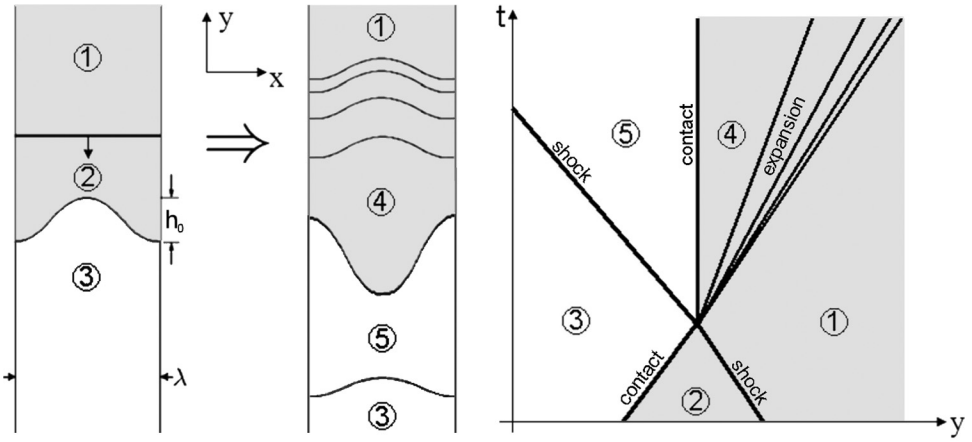

FIG. 2. (a) Schematic depiction of Richtmyer-Meshkov instability for the case in which the shock starts in the heavy fluid, resulting in perturbed reflected expansion and transmitted shock waves. (b) Schematic depiction of the *y-t* diagram for the associated one-dimensional Riemann problem.

Mach numbers to making comparison for amplitude and growth rate in Subsection VIII A.

II. EQUATION OF STATE BACKGROUND

When modeling materials undergoing a process involving a single strong shock, it is useful to build an equation of state from a central Hugoniot.[1–33] A completely general formulation of pressure as a function of density and a partial derivative with respect to internal energy

$$p(\rho,e)=p_{ref}(\rho)+\rho\int_{e_{ref}(\rho)}^{e}\Gamma(\rho,e')de', \tag{1}$$

provides a practical approach for defining the behavior of a material near a known reference state curve. Here, $p_{ref}(\rho)$ and $e_{ref}(\rho)$ are density parameterized reference state curves and $\Gamma(\rho,e)$ is the Grüneisen parameter

$$\Gamma(\rho,e)=\frac{1}{\rho}\frac{\partial p}{\partial e}\bigg|_{\rho}. \tag{2}$$

The functions $p_{ref}(\rho)$ and $e_{ref}(\rho)$ need not be derived from a Hugoniot, however, use of a Hugoniot is generally the most practical choice. For application to modeling many solids, an analytic approximation to a shock Hugoniot can be achieved by noting that experimental data often exhibit a polynomial relationship between shock and particle speed.[1,2,28,29] Presently, the assumption of a linear shock-particle speed relationship is used

$$u_s=c_0+\sigma u_p, \tag{3}$$

where u_s denotes the shock's speed, u_p the post-shock particle speed, c_0 the unshocked medium's speed of sound, and σ is related to the unshocked medium's isentropic pressure derivative of the bulk modulus

$$\begin{aligned} K_s &= \frac{\partial \ln(p)}{\partial \rho}\bigg|_s, \\ \sigma &= \left(\frac{\partial K_s}{\partial p}\bigg|_s+1\right)\Big/4. \end{aligned} \tag{4}$$

Starting from state ρ_0, p_0, and e_0, with the assumed linear shock-particle speed relation and the Rankine-Hugoniot jump conditions

$$\begin{aligned} \rho &= \rho_0 u_s/(u_s-u_p), \\ p &= p_0+\rho_0 u_s u_p, \end{aligned} \tag{5}$$

and

$$e = e_0+\frac{1}{2}(p+p_0)(1/\rho_0-1/\rho), \tag{6}$$

the shock Hugoniot in terms of internal pressure and energy parametrized as functions of density is obtained

$$p_H(\rho)=p_0+\frac{c_0^2(1/\rho_0-1/\rho)}{[1/\rho_0-\sigma(1/\rho_0-1/\rho)]^2}, \tag{7}$$

$$e_H(\rho)=e_0+\frac{1}{2}(p_H(\rho)+p_0)(1/\rho_0-1/\rho). \tag{8}$$

To complete the equation of state for compressed states with $\rho>\rho_0$, $\Gamma(\rho,e)$ is then required. Close to the Hugoniot, many solids exhibit a nearly constant or heavily density dependent Grüneisen parameter, often approximated by

$$\begin{aligned} \Gamma(\rho,e) &= \Gamma_0\left(\frac{\rho_0}{\rho}\right)^q \\ &= \Gamma_H(\rho). \end{aligned} \tag{9}$$

The assumption that the Grüneisen parameter depends only on density leads to the Mie-Grüneisen equation of state form

$$p(\rho,e)=p_{ref}(\rho)+\rho\Gamma_{ref}(\rho)(e-e_{ref}(\rho)). \tag{10}$$

When $\rho<\rho_0$, Eqs. (7) and (8) are not valid. For robustness, the equation of state is sometimes extended for expanded states through use of a second order isentropic continuation to the Hugoniot known as a Murnaghan isentrope[30]

$$p_H(\rho)=\left(p_0+\frac{\rho_0 c_0^2}{4\sigma-1}\right)\left(\frac{\rho}{\rho_0}\right)^{4\sigma-1}-\frac{\rho_0 c_0^2}{4\sigma-1}, \tag{11}$$

$$e_H(\rho)=e_0+\int_{\rho_0}^{\rho}\frac{p_H(\rho)}{\rho^2}d\rho. \tag{12}$$

Downloaded 02 Sep 2011 to 131.215.220.186. Redistribution subject to AIP license or copyright; see http://pof.aip.org/about/rights_and_permissions

A. Equation of state limitations

Due to the nature of the assumptions used in formulating isotropic Mie-Grüneisen equation of state for solids examined Sec. II, several limitations apply. Most notably, the assumed linear shock-particle speed relationship causes a singularity in the equation of state, yielding a non-physical maximum density

$$\rho_{max} = \frac{\rho_0}{1 - 1/\sigma}, \tag{13}$$

Additionally, analysis of isentropes created by the Murnaghan extension of the Hugoniot for expanded states results in a non-physical minimum pressure

$$p_{min} = \frac{-\rho_0 c_0^2}{4\sigma - 1}. \tag{14}$$

Furthermore, although numerically a physical value for the sound speed may still be obtained, a zero temperature limitation may be considered. With presumed constant specific heat, the above three limitations that are depicted in the pressure-density plane in Figure 3 are attainable. With $\rho_0 > 0$, $c_0 > 0$, and $\sigma > 0$, it is clear that $p_{min} < 0$ is typical and therefore negative pressure or tension is permissible. It is useful to place a tensile strength limitation when tension is expected in a simulation. Additionally, positivity of absolute temperature must not be violated. Taking constant specific heat for Aluminum yields Figure 3, giving some face to the expected $p - \rho$ plane of validity.

B. Mixture rules

1. Perfect gas mixture

The kinetic theory for ideal gas mixtures predicts that total pressure is described by partial pressure summation.[31] For mixtures of perfect gases, this law is easily applied to form an analytic equation of state[32]

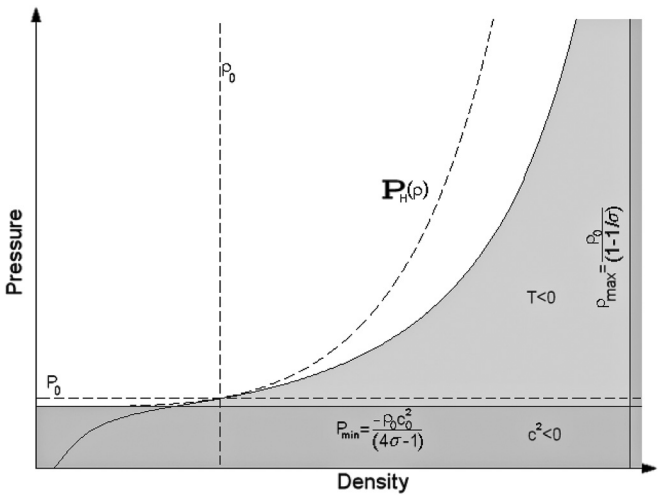

FIG. 3. Forbidden and allowed state regions of the Mie-Grüneisen equation of state formulated from a linear shock-particle speed central shock Hugoniot and Murnaghan isentrope extension for expanded states. The available states are bounded by negative temperature, a nonphysical minimum pressure, and a nonphysical maximum density.

$$p = (\bar{\gamma} - 1)\rho e, \tag{15}$$

with

$$\bar{\gamma} = \sum_{i=1}^{n} y_i c_p^i \Big/ \sum_{i=1}^{n} y_i c_v^i, \tag{16}$$

where y_i, c_p^i, and c_v^i are the ith components mass fraction and specific heats, respectively. Presently, the above mixture rule for perfect gases is applied in simulations.

2. Mie-Grüneisen mixture

For most real materials, a simple theory for molecular interactions in mixtures does not exist. Furthermore, many multiphase flows involving real materials of interest are generally best described as immiscible. However, it has been demonstrated that immiscible Euler flows lead to vortex sheets which are ill-posed and will not yield solution convergence.[25] To avoid solution convergence issues, it is therefore necessary to introduce a miscible mixed phase zone with a finite thickness on the order of a few grid points. Ideally, the behavior of the composite material in the mixed phase zone would be characterized by central Hugoniot data from experiments. Without such data, a composite mixture rule based on a rigorous theory would be desirable. As should be expected, no unique closure to the composite mixture problem exists and the expectation for a simple analytic model is unrealistic.

In the absence of a rigorous composite model, a simple model satisfying basic immiscible conservation of mass and energy is presently applied.[26] The model relaxes other immiscible mixture constraints related to fundamental derivatives. In this model, the composite phase is assumed to maintain the property of a central Hugoniot with a linear shock-particle speed relation defined by parameters $\bar{\rho}_0$, $\bar{e}_0$, $\bar{p}_0$, $\bar{c}_0$, $\bar{\Gamma}$, and $\bar{\sigma}$ to be defined subsequently. A single scalar immiscible volume fraction ψ_i varying between zero and one is introduced to define the amount of the ith phase at each point.

For an immiscible composite under the assumption of a uniform velocity field, the mean density and internal energy must relate to the volume fraction of the ith component of the composite at the reference state. For Mie-Grüneisen fluids, based on a reference state with a linear shock-particle speed relationship, the conservation of reference state internal energy is entirely irrelevant since e_0^i is an arbitrary and any value can, therefore, be taken. Further relationships for $\bar{\Gamma}$, $\bar{\sigma}$, and $\bar{c}_0$ as a function of volume fraction and state variables for immiscible fluid mixtures can be formulated.[30] Since the miscible case is not physical to begin with and the immiscible case can be approached under grid refinement, the aforementioned immiscible relationships are not used presently and instead a simple miscible composite material is assumed defined by

$$\bar{\phi}_0 = \sum_{i=1}^{n} \psi_i \phi_0^i, \tag{17}$$

Downloaded 02 Sep 2011 to 131.215.220.186. Redistribution subject to AIP license or copyright; see http://pof.aip.org/about/rights_and_permissions

where ϕ_0^i is replaced in the formula by the Hugoniot parameters, ρ_0, p_0, e_0, Γ_0, and σ of the ith component with immiscible volume fraction ψ_i. We emphasize that Eq. (17) is used subsequently only to calculate parameters in a mixed-state model and not the state itself.

III. NUMERICAL METHOD

A. Equations of motion

Here, we briefly describe the presently used equations of motion and their application to multiphase Mie-Grüneisen flows with the mixture model in Eq. (17). For more complete details, see Ref. 6. In two dimensions, under several assumptions, the Euler equations of compressible fluid mechanics form a set of coupled, conservative, hyperbolic partial differential equations

$$\begin{array}{rcl} \frac{\partial \rho}{\partial t} & + & \frac{\partial(\rho u)}{\partial x}+\frac{\partial(\rho v)}{\partial y}=0, \\ \frac{\partial(\rho u)}{\partial t} & + & \frac{\partial(\rho u^2+p)}{\partial x}+\frac{\partial(\rho uv)}{\partial y}=0, \\ \frac{\partial(\rho v)}{\partial t} & + & \frac{\partial(\rho uv)}{\partial x}+\frac{\partial(\rho v^2+p)}{\partial y}=0, \\ \frac{\partial(\rho E)}{\partial t} & + & \frac{\partial(u(\rho E+p))}{\partial x}+\frac{\partial(v(\rho E+p))}{\partial y}=0, \end{array} \tag{18}$$

where $E=e+\frac{1}{2}(u^2+v^2)$ is the energy per unit mass. To extend these equations for multiphase flows, an additional scalar ψ_i associated with the ith phase is tracked by the advection equation

$$\frac{\partial \psi_i}{\partial t}+u\frac{\partial \psi_i}{\partial x}+v\frac{\partial \psi_i}{\partial y}=0. \tag{19}$$

Presently, the initial conditions for ψ_j are taken to be the initial volume fraction for Mie-Grüneisen fluids and the mass fraction for perfect gases.

In addition to Eqs. (18) and (19), for Mie-Grüneisen fluids, three redundant density functions associated with the central Hugoniot are tracked by

$$\begin{array}{rcl} \frac{\partial}{\partial t}\left(\frac{1}{\Gamma_H}\right) & + & u\frac{\partial}{\partial x}\left(\frac{1}{\Gamma_H}\right)+v\frac{\partial}{\partial y}\left(\frac{1}{\Gamma_H}\right)=-\rho\chi_{\Gamma_H}\left(\frac{\partial u}{\partial x}+\frac{\partial v}{\partial y}\right), \\ \frac{\partial}{\partial t}\left(\frac{p_H}{\Gamma_H}\right) & + & u\frac{\partial}{\partial x}\left(\frac{p_H}{\Gamma_H}\right)+v\frac{\partial}{\partial y}\left(\frac{p_H}{\Gamma_H}\right)=-\rho\chi_{p_H}\left(\frac{\partial u}{\partial x}+\frac{\partial v}{\partial y}\right), \\ \frac{\partial(\rho e_H)}{\partial t} & + & u\frac{\partial(\rho e_H)}{\partial x}+v\frac{\partial(\rho e_H)}{\partial y}=-\rho\chi_{e_H}\left(\frac{\partial u}{\partial x}+\frac{\partial v}{\partial y}\right), \end{array} \tag{20}$$

where

$$\chi_{\Gamma_H}=-\Gamma_H'/{\Gamma_H}^2, \tag{21}$$

$$\chi_{p_H}=(\Gamma_H p_H'-\Gamma_H' p_H)/{\Gamma_H}^2, \tag{22}$$

$$\chi_{e_H}=e_H+\rho e_H', \tag{23}$$

and prime quantities indicate derivative with respect to density. For example, from Eq. (9)

$$\Gamma_H'=\frac{d\Gamma_H}{d\rho}=-\bar{q}\bar{\Gamma}_0\bar{\rho}_0^{\bar{q}}\rho^{-\bar{q}-1}, \tag{24}$$

with the mixture rule of Eq. (17) used to calculate $\bar{\Gamma}_0$, $\bar{\rho}_0$, and $\bar{q}$ from the current value for $\psi(x,y,t)$. Pressure can then be obtained directly through the relationship

$$p=\left(\rho E-\frac{(\rho u)^2+(\rho v)^2+(\rho w)^2}{2\rho}+\frac{p_H}{\Gamma_H}-\rho e_H\right)\Big/\left(\frac{1}{\Gamma_H}\right). \tag{25}$$

The addition of Eqs. (20) helps to alleviate numerical, phase-error driven, catastrophic oscillations that can occur for mixed phase points.[24,26] For Mie-Grüneisen equation of state, the final tracked, phase-averaged, vector of state is then

$$\mathbf{q}=(\rho,\rho u,\rho v,\rho w,\rho E,1/\Gamma_H,p_H/\Gamma_H,\rho e_H,\psi_1,\ldots,\psi_{n-1}). \tag{26}$$

B. Finite-difference method

Most existing methodologies proposed to address issues specific to the Mie-Grüneisen equation of state are considerably diffusive in nature.[26,30,33] In addressing this issue, we have developed a hybrid methodology that combines a kinetic-energy preserving center-difference approach[34] with a Roe linearized Riemann solver[26] by way of a local smoothness dependent limiter.[6] In brief, a numerical derivative operator is defined by a difference of reconstructed quantities

$$\frac{\partial f}{\partial x}=\frac{\hat{f}_{j+1/2}-\hat{f}_{j-1/2}}{\Delta x}+O(\Delta x^k), \tag{27}$$

where $\hat{f}_{j+1/2}$ is defined by a limiter blending of a fourth-order center-difference and Roe-linearized Riemann solver reconstruction

$$\hat{f}_{j+1/2}=\hat{f}_{j+1/2}^{4^{th}}+\Phi(\hat{f}_{j+1/2}^{Roe}-\hat{f}_{j+1/2}^{4^{th}}). \tag{28}$$

The limiter is defined by

$$\Phi=\|A\|_p\,\|\underline{w}-\underline{C}^r\|_p, \tag{29}$$

the p norm of the deviation of local weighted essentially non-oscillatory (WENO) smoothness weights $\underline{w}$ from their ideal values $\underline{C}^r$. Temporal discretization is achieved by third-order total variation diminishing (TVD) Runge-Kutta.[35] Code verification for manufactured simple wave solutions was performed,[6] demonstrating fourth-order spatial convergence.

Implementation of the solver has been performed utilizing the California Institute of Technology's VTF AMROC[4,5,27] software with adaptive mesh refinement (AMR) capability. The code uses the block structured adaptive mesh refinement (SAMR) algorithm developed by Berger and Coellela[36] for Cartesian meshes, refining equally in both space and time. The amount of local refinement is determined based on local gradient tolerances of quantities.

C. Convergence testing

A mesh refinement study using adaptive mesh refinement for the "light-to-heavy" case with a Mach 2.5 incident shock was performed to determine the needed effective resolution to capture the mixing layer amplitude effectively.

Downloaded 02 Sep 2011 to 131.215.220.186. Redistribution subject to AIP license or copyright; see http://pof.aip.org/about/rights_and_permissions

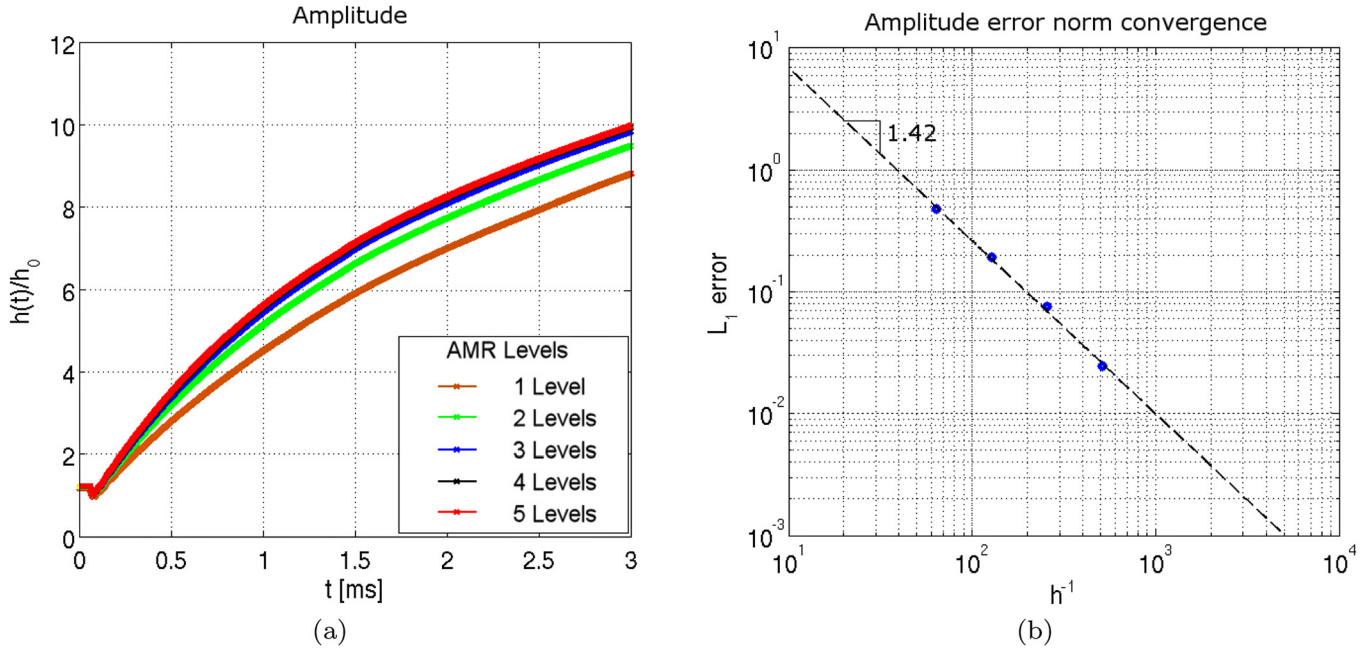

FIG. 4. (Color online) (a) "Light-to-heavy" Mach 2.5 Richtmyer-Meshkov amplitude plot and (b) amplitude convergence plot. The convergence rate is based upon the L_1 norm of the amplitude post-shock corrugation interaction for times up to 1.0 ms.

The results for the study are given in Figure 4 for up to five mesh levels with successive two times refinement for a base mesh of 32 points per corrugation wavelength. To the left, the amplitude is plotted as a function of time and to the right, the L_1 error based on the finest mesh calculation. The size for the mixed cell zone was held constant under refinement. Significant differences in the amplitudes as a function of time are observed between refinements for the first three mesh levels. Between the three- and five-level meshes, less significant change is observed. The convergence rate of the amplitude with effective mesh size is slightly greater than one. Engquist[37] demonstrated that in smooth regions behind discontinuities, the L_1 error convergence rate of any numerical method will be approximately first order.

Therefore for all simulations, a four-level mesh with a base mesh of 32 points per corrugation wavelength and a refinement factor of two for each level beyond the first, corresponding to 256 points per corrugation wavelength was used. Figure 5 demonstrates the behavior of the mesh refinement around the unstable interface created by an incident Mach 1.87 shock in perfect gases with gamma of 1.248 and 1.09, "light" and "heavy," respectively. A Courant-Friedrichs-Lewy (CFL) number of 0.85 was maintained adaptively for all simulations.

D. Initial conditions

In practice, only weak convergence can be obtained for the numerical solution of hyperbolic partial differential equations with discontinuities.[38,39] To obtain smooth solutions, free of oscillations up-winding is generally required at sharp features, leading to numerical diffusion. Furthermore, gradients on the order of the grid scale can sometimes develop into undesirable fluid instabilities. It is, therefore, necessary to smear the initial material contact such that several grid points are present across the mixed zone

$$\rho(x, y, t = 0) = \rho_3 + (\rho_2 - \rho_3)w(y, x), \tag{30}$$

with

$$w(x, y) = \frac{1}{2} + \frac{1}{2}\tanh(\delta(y - y_c(x))), \tag{31}$$

where $y_c(x)$ is the centerline of the mixed region defined by $y_c(x) = h_0 \cos(kx)$. The quantity δ is a parameter which describes the mixed zone width. Presently, it is not the purpose of the study to explore the effect of δ. Therefore, a value which yields a mixed zone of ten points is used simply to prevent gridscale-driven features from developing. Similarly, across the shock, to minimize errors introduced by approximation of the solution to the Riemann problem by linearization, it is useful to smear the shock wave. The shock is then located as close to the corrugated contact as is possible so that quantities in front of the shock are matched to within a hundredth of a percent of those given by the smeared interface. For all simulations, the shock wave starts from above the interface.

In order to maximize efficiency of the domain and mesh utilized, the frame of reference is taken to be that for which the corresponding one-dimensional Riemann problem yields zero velocity for the contact post-shock interaction. Additionally, the initial location of the interface and shock combination is taken such that waves corresponding to the one-dimensional Riemann problem reach the ends of the domain at the same time.

E. Boundary conditions

The domain is chosen to have a large aspect ratio so as to minimize interaction of the flow field at the material interface with the boundary. Additionally, when necessary, the domain is truncated to eliminate shock wave interaction with

Downloaded 02 Sep 2011 to 131.215.220.186. Redistribution subject to AIP license or copyright; see http://pof.aip.org/about/rights_and_permissions

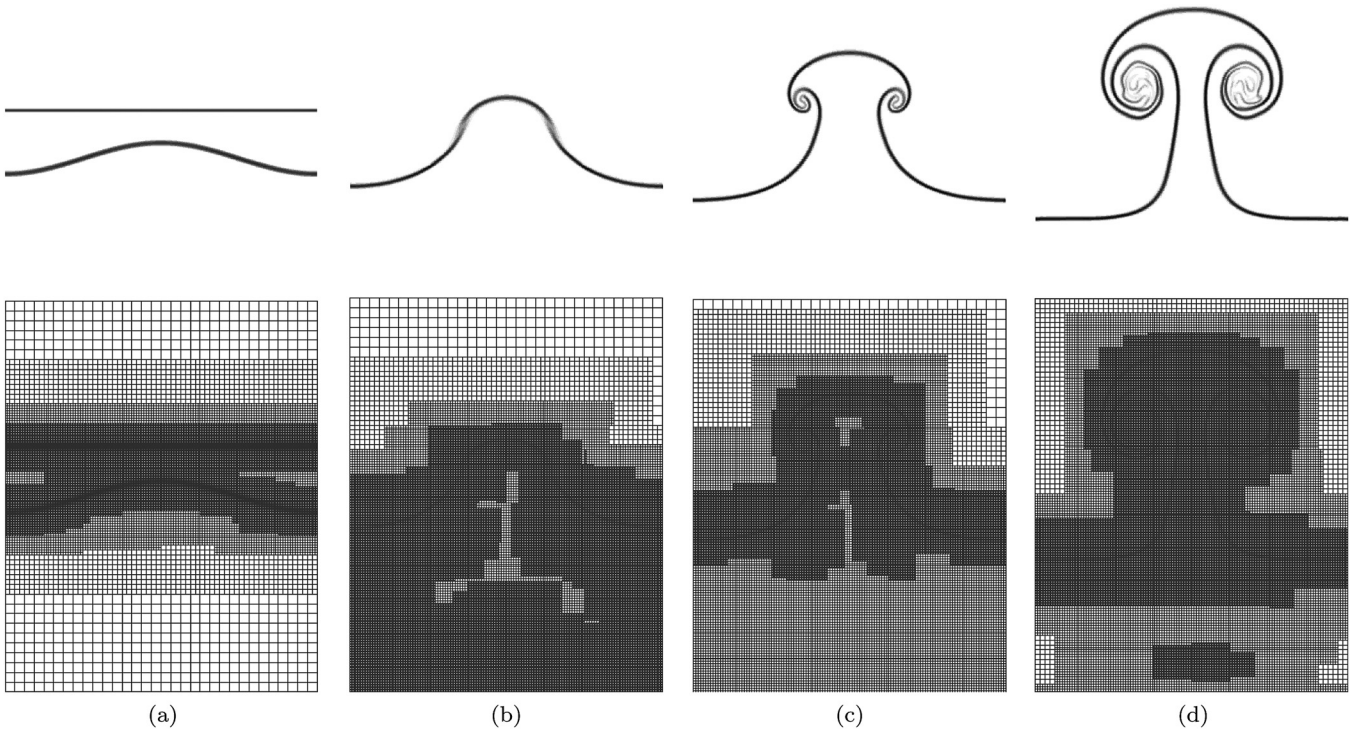

FIG. 5. Light to heavy Mach 1.87 single mode Richtmyer-Meshkov instability Schlerin plots and mesh plots for times (a) −0.075, (b) 1.225, (c) 2.69, and (d) 6.1 ms.

the top and bottom boundaries. In the horizontal direction, the domain is taken to be periodic in nature. Ghost cells are used to implement the periodic boundary conditions in an AMR context. The top and bottom of the domain utilize simultaneous approximation term (SAT) (Ref. 40) with nonreflecting outflow.[41,42]

IV. BACKGROUND THEORY

A. Impulsive model

Early attempts to model Richtmyer-Meshkov instability[7,8] focused on solution to a linearization of the incompressible potential flow equations applied to the impulsive acceleration of a small amplitude corrugation of zero thickness between two fluids. A simple prediction for early time amplitude growth is arrived at from the model

$$h(t) = h_0^+(1 + kA^+\Delta vt), \tag{32}$$

where, for application to modeling Richtmyer-Meshkov instability generated by an incident shock wave, h_0^+ is the post-shock corrugation amplitude, $A^+ = (\rho_4 - \rho_5)/(\rho_4 + \rho_5)$ is the post-shock Atwood ratio, $k = 2\pi/\lambda$ is the corrugation wave number, and Δv is the change in velocity of the interface imparted by the shock associated with the zero-corrugation problem. The linearization of flow equations used to achieve this result assumes that $kh_0^+ \ll 1$. The corresponding prediction for the amplitude growth rate is given by

$$\dot{h}_\infty = h_0^+ kA^+\Delta v. \tag{33}$$

Additionally, through simple geometric consideration, Richtmyer[7] predicted that the amplitude of the corrugation post-shock interaction should be

$$h_0^+ = h_0(1 - \Delta v/V_{s_1}), \tag{34}$$

where V_{s_1} is the incident shock speed relative to the corrugated contact.

Although the classical predictions of Eqs. (32)–(34) remain important in understanding the underlying phenomenon, the assumptions used in achieving them lead to a narrow range of validity in application to shock driven Richtmyer-Meshkov instability. A great deal of further analytic work has been performed to shed light Richtmyer-Meshkov instability. This work goes beyond the scope and point of our present intentions. We refer readers to the original sources of these more complex models.[13–17]

B. Start-up time

Lombardini[12] has developed a modified impulsive model that takes into account the affect of a reflected and transmitted shock on the instability start-up phase. The model utilizes perturbation methods under the assumption that the parameter

$$\varepsilon_j = \frac{kh_0^+}{2\pi}A^+\frac{\Delta v}{a_j}, \tag{35}$$

is small ($\varepsilon_j \ll 1$), for $j = 1, 2$ with aj the speed of sound on either side. The transmitted and reflected shock waves are treated as moving boundaries, shown to play a key roll for early times by limiting the effective size of the domain. The theory falls short of making a prediction for the growth rate of the instability. However, the model does provide a useful prediction for the start-up time constant of the instability

Downloaded 02 Sep 2011 to 131.215.220.186. Redistribution subject to AIP license or copyright; see http://pof.aip.org/about/rights_and_permissions

$$\tau = \frac{1}{2k}\left(\frac{1-A^+}{V_{s_4}} + \frac{1+A^+}{V_{s_5}}\right). \tag{36}$$

Here, V_{s_4} and V_{s_5} are the reflected and transmitted shock speeds, respectively, in the frame of reference in which the zero-corrugation problem yields a stationary contact. For early times, the mixing layer growth rate is predicted to evolve as

$$\dot{h}(t) = \dot{h}_\infty t/\tau. \tag{37}$$

C. Nonlinear regime model

Transition to nonlinear growth occurs as the mixing layer width becomes large in order of magnitude relative to the wavelength ($kh(t) \sim 1$). A variety of attempts to analytically describe the behavior of this nonlinear phase have been made.[17,43–49] Among these are incompressible potential flow models focused on predicting the behavior of the flows large-scale coherent structure based on an incompressible treatment of the flow localized to the bubble or spike tip.[17,43,45–47] Fourier series expansion for the velocity potential is utilized in such models yielding a set of coupled ordinary differential equations. Solution to the system generally predicts an asymptotic bubble velocity inversely proportional to time[43]

$$v_b(t) \to \frac{3+A_0^+}{3(1+A_0^+)kt}. \tag{38}$$

The evolution of the bubble position is thus predicted to be logarithmic in time.

V. MATCHED PARAMETERS

The set of dimensional parameters describing any flow can be subdivided into three categories: coordinate, initial condition, and equation of state parameters. In a stationary Cartesian coordinate system, the first category is composed of space and time variables

$$(x, y, z, t). \tag{39}$$

For single-mode, planar Richtmyer-Meshkov instability, the initial condition is described by three thermodynamic states and three spatial lengthscales associated with the corrugation. Remaining consistent with the labeling of Figures 1 and 2, the-dimensional initial condition parameter family is

$$(p_1, \rho_2, p_2, \rho_3, \lambda, h_0, \delta). \tag{40}$$

Here, δ has been added to describe the lengthscale of the mixed-phase zone where the two materials meet at the corrugation. The state behind the shock is only described by one thermodynamic variable because it must lie on the Hugoniot of the state ahead. Additionally, the pressure across the corrugation is continuous and therefore one less thermodynamic quantity is required. It is important to note that thermodynamic variables are interchangeable, and therefore, the choice of density and pressure used to describe the initial states is not unique.

With fixed equations of state, the initial condition and coordinate parameters provide a basis for a set of nondimensional quantities that define complete similarity between flows. However, presently, the goal is to compare Richtmyer-Meshkov instability across equations of state. For perfect gases a and b, the specific heats

$$(c_p^a, c_v^a, c_p^b, c_v^b) \tag{41}$$

form the set of-dimensional equation of state dependent parameters. These can be reduced to three nondimensional parameters, the specific heat ratios

$$(\gamma^a, \gamma^b, c_v^a/c_v^b), \tag{42}$$

required to be matched for complete flow similarity. Alternatively, for two linear shock-particle speed Hugoniot based Mie-Grüneisen equations of state, the list of dimensionless parameters is much longer

$$\left(\frac{p_0^a}{\rho_0^a c_0^{a2}}, \Gamma_0^a, \sigma^a, \frac{p_0^b}{\rho_0^b c_0^{b2}}, \Gamma_0^b, \sigma^b\right). \tag{43}$$

Although some correlation can be drawn between Γ_0 and γ, there is no clear cut meaning for σ since perfect gases do not have at least one Hugoniot with a linear shock-particle speed relationship. Achieving complete flow similarity across equations of state is, therefore, not a realistic goal, providing motivation for the present study. A weaker form of similarity must then be applied as a basis for comparison.

Of fundamental interest to the study of Richtmyer-Meshkov instability is the mixing layer width time evolution $h(t)$. Presently, the mixing layer width time evolution is taken as the basis for comparison across equations of state. With the equation of state fixed, Buckingham's pi theorem can be utilized to define a nondimensional form of the instability amplitude strictly as a function of nondimensional initial conditions and time. The-dimensional parameters of interest are

$$(h(t), t, p_1, \rho_2, p_2, \rho_3, \lambda, h_0, \delta). \tag{44}$$

There are three fundamental physical quantities among these nine variables (length, time, mass). Therefore, six nondimensional groups can be formed

$$\frac{h}{\lambda}\left(\frac{t}{\lambda}\sqrt{\frac{p_2}{\rho_2}}\right) = \frac{h}{\lambda}\left(\frac{t}{\lambda}\sqrt{\frac{p_2}{\rho_2}}, \frac{p_1}{p_2}, \frac{\rho_2}{\rho_3}, \frac{h_0}{\lambda}, \frac{\delta}{\lambda}\right). \tag{45}$$

Even when limited to the dimensional parameters in Eq. (44), these six groups are not unique. Furthermore, there is no reason to believe that matching such parameters across equations of state will yield any similarity in the nondimensional mixing layer width evolution.

To formulate a more meaningful set of nondimensional parameters, it is useful to draw on theory of Richtmyer-Meshkov instability. Richtmyer's linear theory provides a

Downloaded 02 Sep 2011 to 131.215.220.186. Redistribution subject to AIP license or copyright; see http://pof.aip.org/about/rights_and_permissions

direct prediction for the post-shock evolution of the nondimensional mixing layer width

$$\frac{h}{\lambda}\left(\frac{t}{\tau}\right) = \frac{h_0^+}{\lambda}\left(1+\frac{t}{\tau}\right), \tag{46}$$

where the time scale is given by

$$\tau = (kA^+\Delta v)^{-1}. \tag{47}$$

The quantities Δv and A^+ are theoretical predictions for one-dimensional Riemann problems and are, therefore, strictly related to the thermodynamic states of the initial conditions. Likewise, Richtmyer's linear theory predicts the quantity h_0^+ directly from the initial thermodynamic states and corrugation shape. So long as the final number of nondimensional parameters remains the same, the-dimensional quantities predicted to be of importance by Richtmyer's linear theory can, therefore, be interchanged with those in Eq. (45). The resulting nondimensional parameter family should be a better approximation to those necessary to achieve similar nondimensional mixing layer width evolution across flows with different equations of state. Proceeding in this fashion, the nondimensional time evolution of the mixing layer width can be recast in the functional form

$$\frac{h}{\lambda}(kA^+\Delta v t) = \frac{h}{\lambda}\left(kA^+\Delta v t, \frac{\Delta p}{\rho a_2^2}, A^+, kh_0^+, k\delta\right). \tag{48}$$

In addition to Richtmyer's linear theory, the incident shock strength, originally formulated nondimensionally in terms of the ratio of pressures across the shock, has been replaced by the more robust nondimensional measure of pressure change.

The procedure for setting up matched simulations defined by Eq. (48) is now described. First, two Mie-Grüneisen fluids are chosen, one "heavy" and one "light." An incident shock Mach number and initial corrugation shape kh_0 are then chosen. From the Mach number, the nondimensional pressure jump across the incident shock is determined along with the predicted post-shock Atwood ratio A^+, velocity impulse Δv, and post-shock corrugation shape kh_0^+. From these quantities, an iterative process to determining the appropriate perfect gases for matching is undertaken. The additional physical constraint of thermodynamic equilibrium is imposed across the corrugation of the perfect gases. An initial guess for the properties of the gases is made from the Atwood ratio which only depends on the specific heats. The incident shock strength is matched and then an iterative process involving the solution to the uncorrelated Riemann problem is performed to determine the final properties of the perfect gases needed to match the nondimensional values (49) associated with the Mie-Grüneisen fluids.

TABLE I. Hugoniot constants for various materials. For further shock-particle, Hugoniot constants refer to 1, 2, 28, and 29.

	ρ_0 (kg/m^3)	p_0	Γ_0	$\Gamma_0\, c_0$ (m/s)	σ	q	T_0 (K)
Aluminum	2785	0.0	2.0	5328	1.338	1.0	298
MORB	2660	0.0	1.18	2100	1.68	1.0	1673
Molybdenum	9961	0.0	1.56	4700	1.43	1.0	1673

TABLE II. Initial conditions for single-mode Richtmyer-Meshkov instability in the "light-to-heavy" case for Mie-Grüneisen and perfect gas equations of state.

MORB-molybdenum				
M_s	$\Delta p/\rho_0 c_0^2$	kh_0	A^-	A^+
1.5	0.893	0.10π	0.578	0.479
2.5	4.464	0.10π	0.578	0.438
Perfect gas				
M_s	$\Delta p/\rho_0 c_0^2$	kh_0	A^-	A^+
1.225	0.893	0.12π	0.455	0.479
1.87	4.464	0.17π	0.359	0.438

VI. "LIGHT-TO-HEAVY" SINGLE MODE

To examine the roll of the equation of state in Richtmyer-Meshkov instability, we first study the single mode "light-to-heavy" case. In order to achieve an Atwood ratio of roughly a half, mid-ocean ridge basalt (MORB) and molybdenum were chosen for the materials with Mie-Grüneisen equation of state. The Hugoniot constants for these two materials are found in Table I. For perfect gases, Air and SF6 were taken as a starting point, the later being modified in properties to achieve the matched post-shock Atwood ratio. The two Mach numbers 1.5 and 2.5 were arbitrarily chosen for the MORB and molybdenum case to provide a basis for comparison in parameter space. An initial corrugation amplitude of 5% of the wavelength for MORB and molybdenum was taken with the intention of yielding a value of kh_0^+ sufficient to result in a brief linear growth period. Tabulation of initial conditions and relevant post-shock quantities for zero-corrugation are found in Table II. The unshocked prefect gases are taken to be at approximately room temperature and pressure (T=300 *K*, p=1 atm). Similarly, the unshocked Mie-Grüneisen fluids are in thermodynamic equilibrium at (ρ_0, p_0), respectively. Below the entries for MORB and molybdenum are tabulation of initial and post-shock conditions as well as properties for the corresponding perfect gas cases (Table III), matched in the manner proposed in Sec. V.

Figure 6 shows density gradient magnitude contours for the Mach 1.5 case and matched perfect gas, respectively, at several matched nondimensional times. At each time the perfect gas solution, seen on the right of each sub figure, demonstrate a significantly smaller mixing layer width compared to the corresponding Mie-Grüneisen solutions to the left. For later times, significant variation is observed from one case to another in the shapes of the material contact, particularly in the roll up. We omit similar contour plots for the Mach 2.5 case as they reveal similar observations to those of the Mach

TABLE III. Perfect gas properties for single-mode Richtmyer-Meshkov instability in the "light-to-heavy" case.

Perfect gas properties				
M_s	γ_1	c_{v_1} (kJ/kgK)	γ_2	c_{v_2} (kJ/kgK)
1.225	1.248	7.17	1.09	7.40
1.87	1.248	7.17	1.09	9.32

Downloaded 02 Sep 2011 to 131.215.220.186. Redistribution subject to AIP license or copyright; see http://pof.aip.org/about/rights_and_permissions

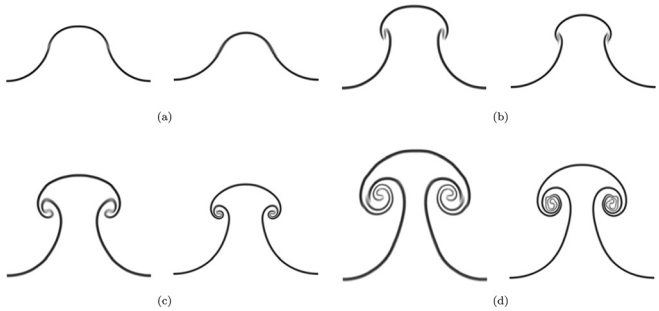

FIG. 6. Light to heavy MORB-molybdenum (left) and equivalent perfect gas (right) single mode Richtmyer-Meshkov instability Schlerin plot comparison for Mach 1.5 incident shock at nondimensional times (a) 3.28, (b) 6.56, (c) 9.834, and (d) 16.39.

1.5 case, with only slightly greater variation in the overall coherent structure.

A. Amplitude and growth rate

Of fundamental interest to the study of Richtmyer-Meshkov instability is the mixing layer width and its growth rate. We present results for these quantities in the current section. Various definitions exist for mixing layer amplitude.[11,50] We define amplitude by a position weighted integral of the initial volume fraction for solids modeled by isotropic Mie-Grüneisen equations of state and mass fraction for perfect gases. Before roll up occurs, we define the interfaces centerline as

$$y_{cd}(x,t) = \frac{\int_{-\infty}^{\infty} y\psi(x,y,t)(1-\psi(x,y,t))dy}{\int_{-\infty}^{\infty} \psi(x,y,t)(1-\psi(x,y,t))dy}, \tag{49}$$

where ψ is the initial volume fraction. The instability amplitude is then

$$h(t) = \frac{1}{2}(y_{spike}(t) - y_{bubble}(t)), \tag{50}$$

where $y_{spike}(t)$ and $y_{bubble}(t)$ are

$$\begin{aligned} y_{spike}(t) &= max(y_{cd}(x,t) - y_0(t)), \quad -\tfrac{\lambda}{2} < x < \tfrac{\lambda}{2}, \\ y_{bubble}(t) &= min(y_{cd}(x,t) - y_0(t)), \quad -\tfrac{\lambda}{2} < x < \tfrac{\lambda}{2}, \end{aligned} \tag{51}$$

where $y_0(t)$ denotes the position of the interface for the unperturbed shock-interface problem as a function of time. Although Eq. (49) fails to capture the centerline of the interface for later times when roll-up has occurred, it still provides a useful measure of the amplitude so long as a single transition zone between phases exist along the vertical line passing through the spike and bubble locations.

Utilizing the above definition for amplitude, Figures 7 and 8, respectively, display non-dimensionalized results for Mach 1.5 and 2.5 Richtmyer-Meshkov instability for the MORB-molybdenum "light-to-heavy" case and associated perfect gas matching (Table III). Several differences are observable in these plots. We first note that an apparent difference in start-up times is evident in the amplitude growth plot. The perfect gas case clearly demonstrates a longer start-up time, as is predicted by Eq. (36) through an inverse dependence on wave speed and corrugation wavenumber. Wave speeds in solids tend to be significantly higher than those for gases by an order of magnitude. This, along with the wavenumber adjustment required for matching predicted linear growth rates, account for the shorter delay in the MORB-molybdenum cases. Table IV gives corresponding start-up times as predicted by Eq. (36) under column labeled τ_{1D} and approximate values from two-dimensional results. We do not attempt to measure the start-up time to any accuracy because it implies the existence of a nearly steady state for the linear growth regime, which is not observed in the present growth rate plots. At best, the linear growth regime is brief for the MORB-molybdenum cases. The predicted start-up times still remain close in order of magnitude to the measured values in spite of the lack of a true linear growth phase. Increasing Mach number appears to increase the variation in amplitude between equations of state. At the lower Mach number, aside from the shift due to start up, the amplitude growth of each equation of state appears quite similar. Alternatively, the perfect gas matching for the Mach 2.5 MORB-molybdenum case decays away from its maximum growth rate much faster. Some of the variation in amplitude evolution can be attributed to inaccuracy of the time constant prediction of Richtmyer's simple impulsive model.

The growth rate plots provide important further insight into the behavior of the mixing layer. Clearly evident are

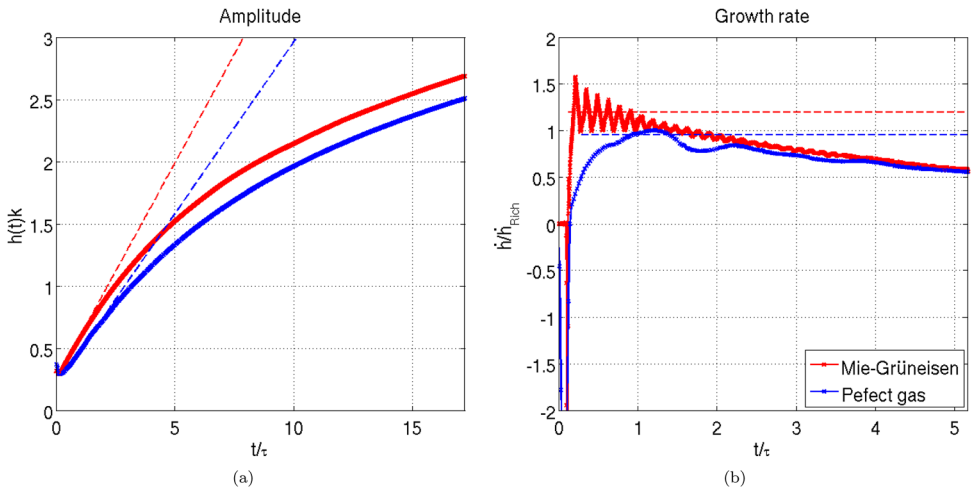

FIG. 7. (Color online) Light to Heavy Mach 1.5 single mode Richtmyer-Meshkov instability amplitude growth plot (a) and amplitude growth rate plot (b). A start-up time difference is clearly observable between the MORB-molybdenum and perfect gas case. Additionally, post start-up the growth rates are observed to oscillate at considerably different frequencies and amplitudes.

Downloaded 02 Sep 2011 to 131.215.220.186. Redistribution subject to AIP license or copyright; see http://pof.aip.org/about/rights_and_permissions

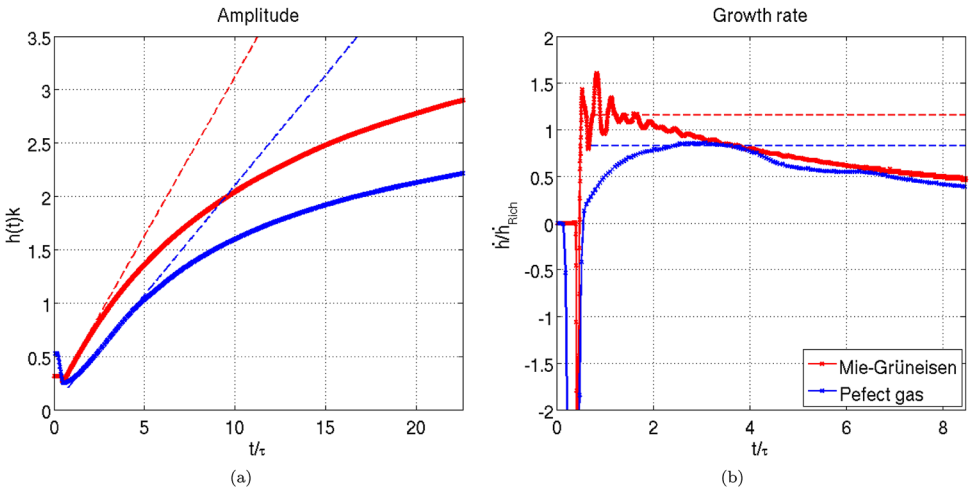

FIG. 8. (Color online) Light to Heavy Mach 2.5 single mode Richtmyer-Meshkov instability amplitude growth plot (a) and amplitude growth rate plot (b). Again, a start-up time difference is clearly observable between the MORB-molybdenum and perfect gas case. Post start-up oscillations in growth rate for MORB-molybdenum are at much greater frequency and amplitudes than those of the perfect gas.

decaying oscillations in growth rate which appear to be nearly constant in frequency for early times. The MORB-molybdenum cases demonstrate a much higher frequency and amplitude of oscillation than the corresponding perfect gas cases. These oscillations are a direct consequence of the perturbed transmitted and reflected shocks. For most materials, small perturbations in shock shape are stable, oscillating, and decaying in time.[51] The oscillation frequency dependence is complex in nature; however, it is directly related to the speed of sound behind the shock and shock perturbation wavenumber[52]

$$(\omega_j - k_y v)^2 = a_j^2 (k_x^2 + k_y^2). \tag{52}$$

Just as in the start-up time, corrugation wavenumber and material wave speeds are seen to play a similar role in determining the frequency of oscillation, yielding a much higher frequency for MORB-molybdenum than the matched perfect gas case. Table V gives approximate values for the oscillation frequencies of the transmitted and reflected shocks based on this formula. Additionally, calculated from a Gaussian filtered polynomial fit of the growth rate after shock-interface interaction is a discrete Fourier transform of the growth rate. Tabulated in Table V are the dominantly observed frequency along with the simple approximation values.

TABLE IV. Start-up times for Richtmyer-Meshkov instability as approximated by zero-corrugation Riemann solution and two-dimensional simulation results.

MORB-molybdenum		
M_s	τ_{1D}/τ	τ_{2D}/τ
1.5	0.0228	~ 0.0328
2.5	0.0738	~ 0.0531
Perfect gas		
M_s	τ_{1D}/τ	τ_{2D}/τ
1.225	0.259	~ 0.393
1.87	1.02	~ 1.32

TABLE V. Nondimensionalized dominant growth rate oscillation frequency $f_{2D}\tau$ for "light-to-heavy" Richtmyer-Meshkov instability and approximate perturbed transmitted and reflected shock oscillation frequency, $f_{T_{1D}}\tau$ and $f_{R_{1D}}\tau$, respectively, based on solution to the zero-corrugation Riemann problem.

MORB-molybdenum			
M_s	$\tau f_{R_{1D}}$	$\tau f_{T_{1D}}$	τf_{2D}
1.5	7.05	7.86	7.06
2.5	3.80	2.39	4.99
Perfect gas			
M_s	$\tau f_{R_{1D}}$	$\tau f_{T_{1D}}$	τf_{2D}
1.225	1.22	0.68	1.06
1.87	0.43	0.25	0.37

B. Nonlinear bubble evolution

Next, we investigate the evolution of the bubble in the nonlinear regime. Figure 9 gives the bubble position as a function of time for Mach 1.5 and 2.5 MORB-molybdenum cases and the equivalent matched perfect gas cases. The plots, given in semi log format, demonstrate a logarithmic nonlinear growth period in all studied cases. The Mach 2.5 matched perfect gas case simulation however, also demonstrates a somewhat unexpected reversal of bubble velocity as

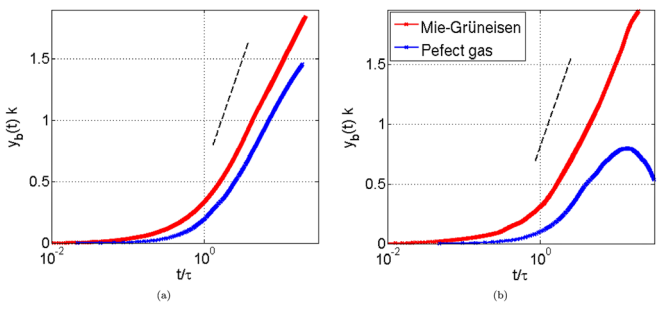

FIG. 9. (Color online) Light to Heavy Mach single mode Richtmyer-Meshkov instability bubble position semi log plot for (a) Mach 1.5 and (b) Mach 2.5 cases. The dashed line in the plots represents Goncharov's potential flow slope prediction for the slope of the logarithmic evolution of the bubble in time.

Downloaded 02 Sep 2011 to 131.215.220.186. Redistribution subject to AIP license or copyright; see http://pof.aip.org/about/rights_and_permissions

TABLE VI. Tabulated comparison of two dimensional bubble evolution parameter in nonlinear regime and Goncharov's nonlinear bubble potential flow approximation.

MORB-molybdenum		
M_s	Simulation	$\frac{3+A^+}{3(1+A^+)}$
1.5	0.558	0.784
2.5	0.686	0.797
Perfect gas		
M_s	Simulation	$\frac{3+A^+}{3(1+A^+)}$
1.225	0.495	0.784
1.87	0.327	0.797

the curvature of the bubble reaches zero. In each of the plots, a dashed line is shown representing the predicted asymptotic slope for the logarithmic time evolution of the bubble by Eq. (38). In each case, the simulation results yield a smaller slope than those of the potential flow prediction (Table VI). The "heavy-to-light" cases later examined demonstrate analogous results, slightly in better agreement with theory, but are thus omitted.

C. Integral vorticity

We now investigate the vorticity distribution as deposited by the shock. For a discontinuous corrugation, the circulation deposited is merely the transverse velocity jump across the different phases. Numerically, it is not possible to measure this; however, since the majority of the vorticity within the domain will be associated with the initial deposition at the contact, we examine an integral of vorticity

$$\Delta u(x,t) = \int_{-\infty}^{\infty} \omega(x,y,t)dy, \tag{53}$$

which is directly related to the tangential velocity jump across the contact. Numerically, we carry out the integration by a trapezoidal rule with differentiation of the velocity field by a *Minmod* limiter.[38,53] We calculate the power spectrum for each distribution by discrete Fourier transform and smooth out the result by a high order least squares polynomial fit of the spectrum's logarithm. Figure 10 displays normalized vorticity distributions and associated power spectrum shortly after shock interaction for MORB-molybdenum Mach 1.5 Richtmyer-Meshkov instability and corresponding perfect gas cases of matched initial conditions. The results for the present Mach 2.5 case and later "heavy-to-light" cases are omitted and demonstrate very similar results. In spite secondary wave effects, the vorticity distribution exhibits the behavior of a sinusoidal distribution with a single mode to within roughly 15%, in reasonable agreement with the prediction of Samtaney and Zabusky,[54]

$$\Delta u(x,t) = \Gamma^+ \sin(\alpha) + O(\sin^2(\alpha)). \tag{54}$$

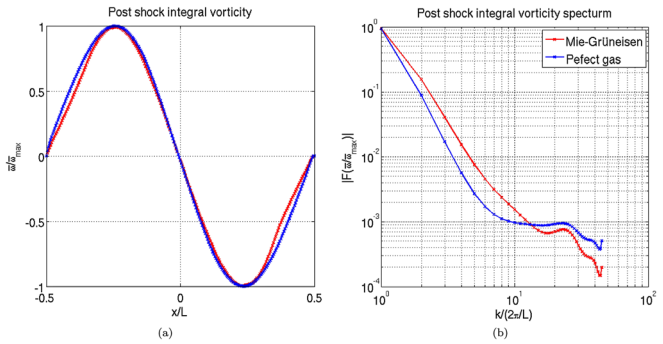

FIG. 10. (Color online) Light to heavy Mach 1.5 single mode Richtmyer-Meshkov instability post-shock integral vorticity plot (a) and integral vorticity power spectrum plot (b). Significant change is observed between equations of state due to the nature of the Hugoniot.

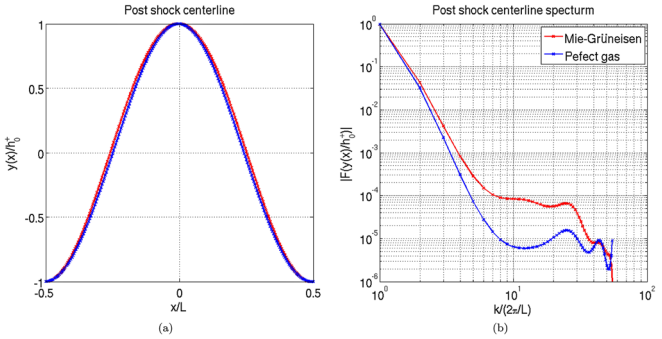

FIG. 11. (Color online) Light to heavy Mach 1.5 single mode Richtmyer-Meshkov instability post-shock centerline plot (a) and centerline power spectrum plot (b). The post-shock centerlines for both equations of state remain for the most part as a single mode.

D. Post-shock interface centerline

We now investigate the post-shock interface centerline as defined by Eq. (49). Figure 11 displays a normalized centerline plot and associated power spectrum shortly after shock interaction for MORB-molybdenum Mach 1.5 and 2.5 Richtmyer-Meshkov instability and corresponding perfect gas cases of matched initial conditions. The centerlines are seen to remain as a single mode to within roughly 5%. Additionally, we note that the post-shock amplitude agrees to within a few percent with the estimate of Eq. (34). The present Mach 2.5 case and following "heavy-to-light" cases demonstrates analogous results which are thus omitted.

VII. "LIGHT-TO-HEAVY" TRIPLE MODE

When multiple modes are present, products of variables in the Euler equations can lead to non-linear reinforcement or interference across modes when two wavenumber sum to a third. We next investigate triple mode Richtmyer-Meshkov instability with the mode coupling $k_1 = k_2 + k_3$, where $k_2 = \frac{2}{3}k_1$, $k_3 = \frac{1}{3}k_1$, and $k_1 h_1 = k_2 h_2 = k_3 h_3$. As a starting point, we retain the wavenumbers from the previous single mode investigation for k_1, but utilize a corrugation amplitude that is 2% of the wavelength. Tabulation of the three initial wavelengths and associated amplitudes are given in Table VII for MORB-molybdenum and perfect gas simulations.

Figure 12 shows density gradient magnitude contours for the present triple mode case and matched perfect gas. Again, the amplitude of the mixing layer for the perfect gas

Downloaded 02 Sep 2011 to 131.215.220.186. Redistribution subject to AIP license or copyright; see http://pof.aip.org/about/rights_and_permissions

TABLE VII. Initial conditions for triple-mode Richtmyer-Meshkov instability in the "light-to-heavy" case for Mie-Grüneisen and perfect gas equations of state.

MORB-molybdenum			
M_s	$k_1 h_1$	k_2/k_1	k_3/k_1
2.5	0.04π	2/3	1/3
Perfect gas			
M_s	$k_1 h_1$	k_2/k_1	k_3/k_1
1.87	0.025π	2/3	1/3

cases is seen to lag behind that of the corresponding MORB-molybdenum cases. Consequently, roll up is delayed in time as well.

A. Amplitude and growth rate

The mixing layer amplitude and growth rate are given in Figure 13. A variation in start-up time of the same order of magnitude as in the single mode case is again observed. A similar order of magnitude variation in growth rate oscillations is also observed. However, three distinct oscillation frequencies are now observed, associated with the three different wavelengths of the corrugation. Tabulation of frequency values is given in Table VIII. Strong correlation is observed between the observed oscillation frequencies and predicted values from the associated zero-corrugation problem. The precise relation between transmitted and reflected shock frequencies and contact oscillation frequency is not known.

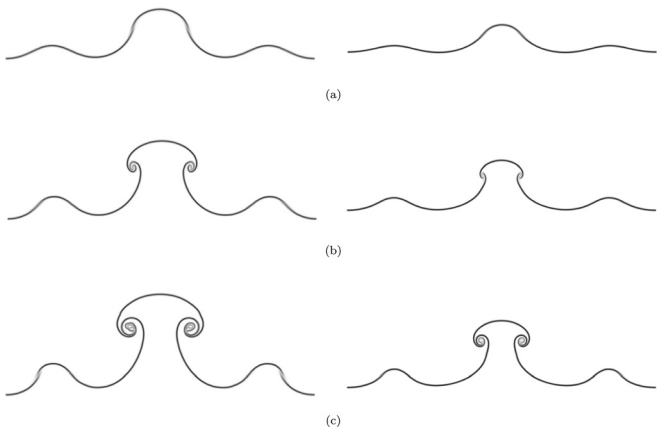

FIG. 12. "Light-to-heavy" MORB-molybdenum Mach 2.5 triple-mode Richtmyer-Meshkov instability schlieren plots and equivalent perfect gas plots for nondimensional times (a) 5.31, (b) 10.6, and (c) 15.9.

TABLE VIII. Dominant growth rate oscillation frequencies τf_{2D} for "light-to-heavy" triple-mode Richtmyer-Meshkov instability and approximate perturbed transmitted and reflected shock oscillation frequency, $\tau f_{T_{1D}}$ and $\tau f_{R_{1D}}$, respectively, based on solution to the zero-corrugation Riemann problem.

	MORB-molybdenum	Perfect gas
$\tau f_{R1_{1D}}$	3.80	0.433
$\tau f_{T1_{1D}}$	2.39	0.245
$\tau f_{1_{2D}}$	3.61	0.371
$\tau f_{R2_{1D}}$	2.54	0.288
$\tau f_{T2_{1D}}$	1.59	0.163
$\tau f_{2_{2D}}$	2.41	0.213
$\tau f_{R3_{1D}}$	1.27	0.144
$\tau f_{T3_{1D}}$	0.80	0.082
$\tau f_{3_{2D}}$	1.26	0.143

VIII. "HEAVY-TO-LIGHT" SINGLE MODE

We next consider the single mode "heavy-to-light" case. We again utilize MORB and molybdenum for the materials with Mie-Grüneisen equation of state and Air and SF6 as a starting point for perfect gases. Mach numbers of 1.5 and 2.5 for the MORB and molybdenum case provide the basis for comparison in parameter space for the "heavy-to-light" case as well. For the Mach 1.5 case, a 5% of the wavelength initial corrugation amplitude was taken as well. For the Mach 2.5 case, due to the large compression of the corresponding perfect gas case interface by the shock that would result, a smaller amplitude of 2% of the wavelength was taken. Tabulation of these initial conditions and relevant post-shock quantities for zero-corrugation are found in Table IX. Again, the unshocked prefect gases are taken to be at approximately room temperature and pressure (T = 300 K, p = 1 atm). Likewise, the unshocked Mie-Grüneisen fluids are in thermodynamic equilibrium at (ρ_0, p_0), respectively (Table IX). The

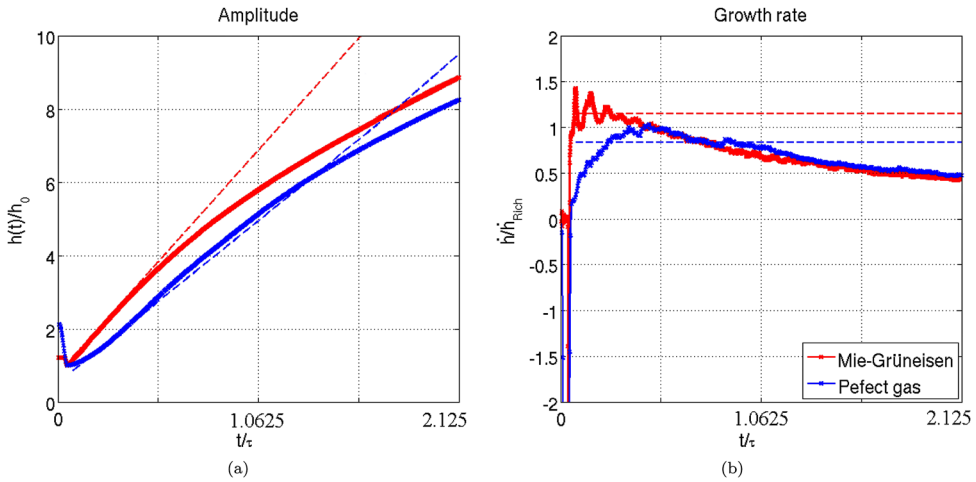

FIG. 13. (Color online) Light to Heavy Mach 2.5 triple mode Richtmyer-Meshkov instability amplitude growth plot (a) and amplitude growth rate plot (b). A start-up time difference is clearly observable between the MORB-molybdenum and perfect gas case. Post start-up oscillations in growth rate for MORB-molybdenum are at much greater frequency and amplitudes than those of the perfect gas.

Downloaded 02 Sep 2011 to 131.215.220.186. Redistribution subject to AIP license or copyright; see http://pof.aip.org/about/rights_and_permissions

entries for MORB and molybdenum are tabulated below (Table IX), including initial and post-shock conditions as well as the properties for the corresponding matched perfect gas cases (Table X).

Figure 14 shows density gradient magnitude contours for the Mach 1.5 case and matched perfect gas, respectively. We again omit the Mach 2.5 case as it demonstrates only a minor variation in the overall coherent structure.

TABLE IX. Initial conditions for single-mode Richtmyer-Meshkov instability in the "heavy-to-light" case for Mie-Grüneisen and perfect gas equations of state.

Molybdenum-MORB				
M_s	$\Delta p/\rho_0 c_0^2$	kh_0	A^-	A^+
1.5	1.049	0.10π	−0.578	−0.437
2.5	5.245	0.04π	−0.578	−0.446
Perfect gas				
M_s	$\Delta p/\rho_0 c_0^2$	kh_0	A^-	A^+
1.244	1.049	0.11π	−0.420	−0.437
1.934	5.245	0.095π	−0.391	−0.446

TABLE X. Perfect gas properties for single-mode Richtmyer-Meshkov instability in the "heavy-to-light" case.

Perfect gas				
M_s	γ_1	c_{v_1} (kJ/kgK)	γ_2	c_{v_2} (kJ/kgK)
1.244	1.248	7.17	1.09	7.17
1.934	1.248	7.17	1.09	8.65

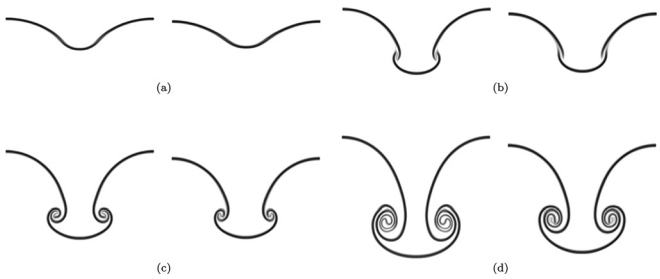

FIG. 14. Heavy to light MORB-molybdenum (left) and equivalent perfect gas (right) single mode Richtmyer-Meshkov instability Schlerin plot comparison for Mach 1.5 incident shock at nondimensional times (a) 3.01, (b) 6.02, (c) 9.02, and (d) 15.04.

A. Amplitude and growth rate

Figures 15 and 16 display non-dimensionalized results for Mach 1.5 and 2.5 Richtmyer-Meshkov instability, respectively, for the MORB-molybdenum "heavy-to-light" case and associated perfect gas matching. The growth rate plots have been scaled by the alternative prediction[55]

$$\dot{h}_\infty = \frac{1}{2}(h_0^- + h_0^+)kA^+\Delta v, \tag{55}$$

which gives better agreement. Unlike the "light-to-heavy" case, a much higher degree of similarity is observed in the features of the growth plots. The most notable difference is that the peak growth rate attained by the perfect gases is considerably less than those of the MORB-molybdenum. Start-up time and growth rate oscillations are all similar in magnitude (Table XI). Evidently, the wavenumber required to yield a matching of growth rate correlates directly to wave speed for the present case. Again, the linear growth regime is not distinctly evident in the present growth rate plots. Just as in the "light-to-heavy" case, the decay in growth rate deviates between equations of state more as the strength of the shock increases, MORB-molybdenum demonstrating a higher decay rate. This is in part due to the larger compression of the perfect gas interface requiring a bigger h_0^- to obtain similar $h_0^+ k$ values, thus yielding a larger linear growth rate for the perfect gas by the prediction of Eq. (55).

B. Incipient weak shock waves

Figure 17 gives density contour plots at several different times for "heavy-to-light" Mach 1.5 Richtmyer-Meshkov instability in MORB-molybdenum. Clearly evident in the contour plots is a transmitted shock and reflected expansion wave. However, an additional and somewhat unexpected series of shock waves are observed to form within the region of the expansion fan. These shock waves first form along the boundary and propagate away from the corrugation. A somewhat analogous phenomenon has been observed in Rayleigh-Taylor instability.[56] For Rayleigh-Taylor instability, Olson and Cook observed that the acceleration of an interface driven by a constant gravitational field generated shocklets, much in the same way a piston does, which eventually catch

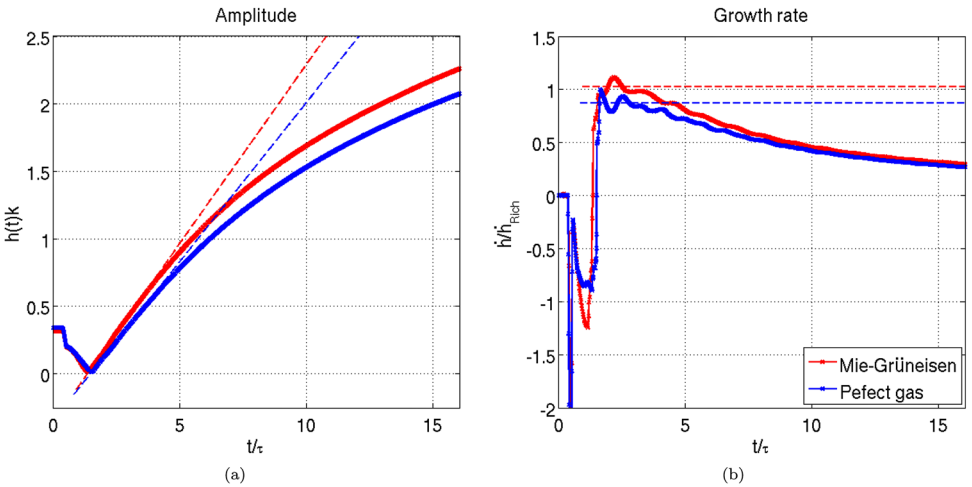

FIG. 15. (Color online) Heavy to light Mach 1.5 single mode Richtmyer-Meshkov instability amplitude growth plot (a) and amplitude growth rate plot (b). The plots show a greater level of similarity than the "light-to-heavy" case. Start-up times are observed to be on the same order of magnitude. Post start-up oscillations in growth rate also demonstrate similar frequencies and amplitudes.

Downloaded 02 Sep 2011 to 131.215.220.186. Redistribution subject to AIP license or copyright; see http://pof.aip.org/about/rights_and_permissions

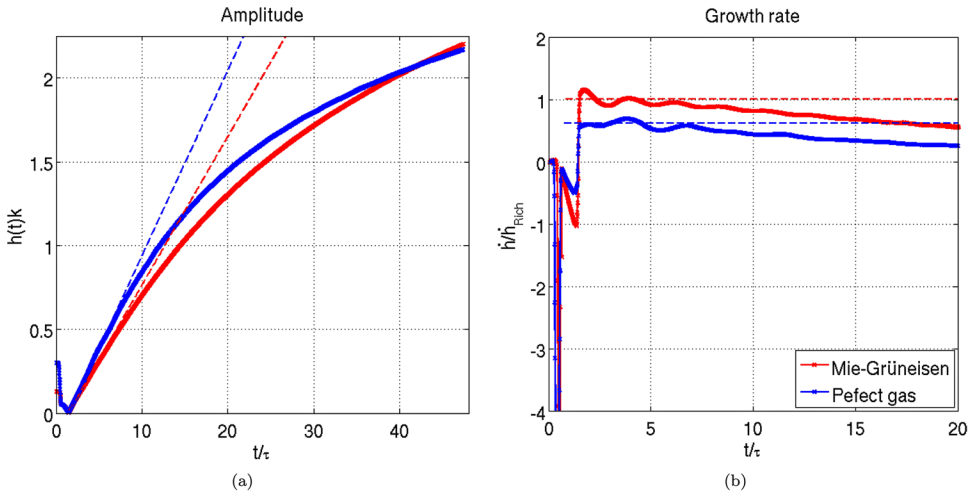

FIG. 16. (Color online) Heavy to light Mach 2.5 single mode Richtmyer-Meshkov instability amplitude growth plot (a) and amplitude growth rate plot (b). Again, tart-up times are observed to be on the same order of magnitude. Post start-up oscillations in growth rate also demonstrate similar frequencies and amplitudes.

TABLE XI. Growth rate oscillation frequency f_{2D} for "heavy-to-light" Richtmyer-Meshkov instability and approximate perturbed transmitted shock oscillation frequency $f_{T_{1D}}$ based on solution to the zero-corrugation Riemann problem.

MORB-molybdenum		
M_s	$\tau f_{T_{1D}}$	τf_{2D}
1.5	1.21	1.21
2.5	1.20	0.49
Perfect gas		
M_s	$\tau f_{T_{1D}}$	τf_{2D}
1.244	1.26	1.22
1.934	0.42	0.38

up to one another to form a weak shock. Presently, in "heavy-to-light" Richtmyer-Meshkov instability, we observe incipient weak shock waves generated by oscillations in the material contact. It is evident that waves produced by the perturbed transmitted shock cause oscillations in the shape of the interface centerline. In the present case of "heavy-to-light" Ricthmyer-Meshkov instability, the strength of these oscillations is strong enough to generate noticeably strong shocks within the heavy material for both Mach 1.5 and 2.5 cases. A similar set of incipient weak shock waves is observable for the corresponding perfect gas cases.

IX. CONCLUSIONS

The present investigation of Richtmyer-Meshkov instability focused on the role of the equation of state. The results for Richtmyer-Meshkov instability in fluids with Mie-Grüneisen equations of state derived from a linear shock-particle speed Hugoniot relationship were compared to those in perfect gases under room temperature and pressure conditions commonly studied. The basis for comparison across equations of state was formulated in terms of Richtmyer's

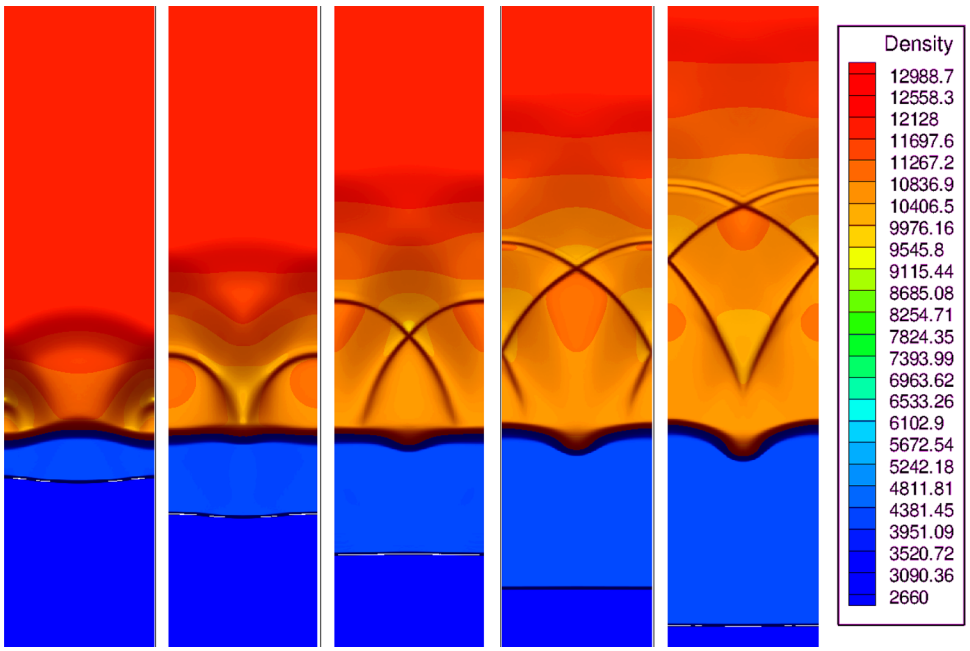

FIG. 17. (Color online) Density contours showing the formation of incipient weak shock waves for Richtmyer-Meshkov instability in MORB-molybdenum modeled by Mie-Grüneisen equations of state for Mach 1.5 in the "heavy-to-light" case. At early times the transmitted shock and reflected expansion are clearly visible. Formation of incipient weak shock waves begins along the edge.

Downloaded 02 Sep 2011 to 131.215.220.186. Redistribution subject to AIP license or copyright; see http://pof.aip.org/about/rights_and_permissions

incompressible theory in nondimensional form. This contains equation of state information implicitly through the predicted time scale that is a function of the post-shock Atwood ratio and a nondimensional pressure jump across the incident, driving shock. As well, to ensure a similar nondimensional mixing layer width evolution, the post-shock amplitude-to-wavelength ratio was matched. Comparison made on this physically relevant basis reveals several noteworthy differences and similarities.

Solids and liquids have sound speeds generally an order of magnitude greater than those of gases. Variation in Richtmyer-Meshkov instability in materials with different wave speed is entirely expected. When a reflected shock occurs, the wave speed is presently observed to play an important role for early time instability growth. This is most evident in the start-up time and growth-rate oscillations which are of order of magnitude different for simulations of Richtmyer-Meshkov instability in MORB and molybdenum with Mie-Grüneisen equations of state when compare to those of perfect gases for the case of a reflected shock. Somewhat unexpected, however, is the absence of such differences observed in the case of a reflected expansion. It is not clear if this is coincidental or a consequence of the parameter matching used. The growth-rate oscillations for all cases are found to be consistent in order of magnitude with a frequency proportional to the speed of sound multiplied by the wavelength. Additionally observed in the "heavy-to-light" cases are a series of incipient weak shocks driven by the oscillation in material contact driven by the perturbed transmitted shock. These first form in the heavy fluid directly above the spike.

For both "light-to-heavy" and "heavy-to-light" cases, variation in the detailed roll-up shape is observed between equations of state. The post-shock center lines are found to agree well, indicating that these differences are driven mostly by variation in the initial vorticity deposited by the shock and the post-shock waves driven by the perturbed reflected and transmitted shocks. Increasing Mach number for the incident shock enhances differences in large scale coherent structures as well as roll-up formation. In the nonlinear regime, the bubble position exhibits a logarithmic variation in time for all cases. At the largest Mach number, the matched perfect gas case exhibits a sudden deviation from this logarithmic behavior as the bubble becomes nearly completely flattened and then reverses direction.

[1]R. Jeanloz, "Shock wave equation of state and finite strain theory," J. Geophys. Res. **94**, 5873, doi:10.1029/JB094iB05p05873 (1989).
[2]R. G. McQueen, S. P. Marsh, J. W. Taylor, J. N. Fritz, and W. J. Carter, "The equation of state of solids from shock wave studies," *High Velocity Impact Phenomena* (Academic Press, New York, 1970), edited by R. Kinslow, Vol. 293, pp. 294–417.
[3]R. Menikoff and B. J. Plohr, "The Riemann problem for fluid flow of real materials," Rev. Mod. Phys. **61**(1), 75 (1989).
[4]R. Deiterding, "Construction and application of an AMR algorithm for distributed memory computers," in *Adaptive Mesh Refinement: Theory and Applications*, edited by T. Plewa, T. Linde, and V. Gregory Weirs, Lecture Notes in Computational Science and Engineering (Springer, Berlin, 2005), Vol. 41, pp. 361–372.
[5]R. Deiterding, "Parallel adaptive simulation of multi-dimensional detonation structures," Ph.D. thesis (Brandenburgische Technische Universität Cottbus, September 2003).
[6]G. M. Ward and D. I. Pullin, "A hybrid, center-difference, limiter method for simulations of compressible multicomponent flows with Mie-Grüneisen equation of state," J. Comput. Phys. **229**, 2999 (2010).
[7]R. D. Richtmyer, "Taylor instability in shock acceleration of compressible fluids," Technical report, LA-1914 (del.), Los Alamos Scientific Lab., N. Mex., 1954.
[8]E. E. Meshkov, "Instability of the interface of two gases accelerated by a shock wave," Fluid Dyn. **4**(5), 101 (1969).
[9]R. L. Holmes, G. Dimonte, B. Fryxell, M. L. Gittings, J. W. Grove, M. Schneider, D. H. Sharp, A. L. Velikovich, R. P. Weaver, and Q. Zhang, "Richtmyer–Meshkov instability growth: Experiment, simulation and theory," J. Fluid Mech. **389**, 55 (1999).
[10]J. W. Grove, R. Holmes, D. H. Sharp, Y. Yang, and Q. Zhang, "Quantitative theory of Richtmyer-Meshkov instability," Phys. Rev. Lett. **71**(21), 3473 (1993).
[11]R. M. J. Kramer, D. I. Pullin, D. I. Meiron, and C. Pantano, "Shock-resolved Navier–Stokes simulation of the Richtmyer–Meshkov instability start-up at a light–heavy interface," J. Fluid Mech. **642**, 421 (2009).
[12]M. Lombardini and D. I. Pullin, "Startup process in the Richtmyer–Meshkov instability," Phys. Fluids **21**, 044104 (2009).
[13]Y. Yang, Q. Zhang, and D. H. Sharp, "Small amplitude theory of Richtmyer–Meshkov instability," Phys. Fluids **6**, 1856 (1994).
[14]J. G. Wouchuk and K. Nishihara, "Asymptotic growth in the linear Richtmyer-Meshkov instability," Phys. Plasmas **4**(4), 1028 (1997).
[15]J. G. Wouchuk, "Growth rate of the linear Richtmyer-Meshkov instability when a shock is reflected," Phys. Rev. E **63**(5), 56303 (2001).
[16]J. G. Wouchuk, "Growth rate of the Richtmyer–Meshkov instability when a rarefaction is reflected," Phys. Plasmas **8**, 2890 (2001).
[17]Q. Zhang and S. I. Son, "An analytical nonlinear theory of Richtmyer-Meshkov instability," Phys. Lett. A **212**(3), 149 (1996).
[18]J. W. Jacobs and J. M. Sheeley, "Experimental study of incompressible Richtmyer–Meshkov instability," Phys. Fluids **8**, 405 (1996).
[19]M. A. Jones and J. W. Jacobs, "A membraneless experiment for the study of Richtmyer–Meshkov instability of a shock-accelerated gas interface," Phys. Fluids **9**, 3078 (1997).
[20]B. D. Collins and J. W. Jacobs, "PLIF flow visualization and measurements of the Richtmyer–Meshkov instability of an air/SF6 interface," J. Fluid Mech. **464**, 113 (2002).
[21]J. W. Jacobs and V. V. Krivets, "Experiments on the late-time development of single-mode Richtmyer–Meshkov instability," Phys. Fluids **17**, 034105 (2005).
[22]C. E. Niederhaus and J. W. Jacobs, "Experimental study of the Richtmyer–Meshkov instability of incompressible fluids," J. Fluid Mech. **485**, 243 (2003).
[23]M. Vetter and B. Sturtevant, "Experiments on the Richtmyer-Meshkov instability of an air/SF6 interface," Shock Waves **4**(5), 247 (1995).
[24]R. Abgrall, "How to prevent pressure oscillations in multicomponent flow calculations: A quasi conservative approach," J. Comput. Phys. **125**(1), 150 (1996).
[25]R. Samtaney and D. I. Pullin, "On initial-value and self-similar solutions of the compressible Euler equations," Phys. Fluids **8**, 2650 (1996).
[26]K. M. Shyue, "A fluid-mixture type algorithm for compressible multicomponent flow with Mie-Gruneisen equation of state," J. Comput. Phys. **171**(2), 678 (2001).
[27]J. Cummings, M. Aivazis, R. Samtaney, R. Radovitzky, S. Mauch, and D. I. Meiron, "A virtual test facility for the simulation of dynamic response in materials," J. Supercomput. **23**(1), 39 (2001).
[28]D. Steinberg, "Equation of state and strength properties of selected materials," Lawrence Livermore National Laboratory Report, UCRL-MA-106439, Livermore, 1996.
[29]L. Rowan, "I. Equation of State of Molten Mid-Ocean Ridge Basalt; II. Structure of Kilauea Volcano," Ph.D. thesis, Ph.D.Dissertation thesis (California Institute of Technology, Pasadena, CA, 1993).
[30]G. H. Miller and E. G. Puckett, "A high-order Godunov method for multiple condensed phases," J. Comput. Phys. **128**(1), 134 (1996).
[31]E. H. Kennard, *Kinetic Theory of Gases* (McGraw-Hill New York, 1938), Vol. 304.
[32]P. A. Thompson and A. A. Sonin, "Compressible-fluid dynamics," Phys. Today **26**, 65 (1973).
[33]G. Allaire, S. Clerc, and S. Kokh, "A five-equation model for the simulation of interfaces between compressible fluids," J. Comput. Phys. **181**(2), 577 (2002).
[34]C. Pantano, R. Deiterding, D. J. Hill, and D. I. Pullin, "A low-numerical dissipation, patch-based adaptive-mesh-refinement method for large-eddy simulation of compressible flows," J. Comput. Phys. **221**, 63 (2006).

Downloaded 02 Sep 2011 to 131.215.220.186. Redistribution subject to AIP license or copyright; see http://pof.aip.org/about/rights_and_permissions

[35]S. Gottlieb, C. W. Shu, and E. Tadmor, "Strong stability-preserving high-order time discretization methods," SIAM Rev. **43**, 89 (2001).
[36]M. J. Berger and P. Colella, "Local adaptive mesh refinement for shock hydrodynamics," J. Comput. Phys. **82**(1), 64(1989).
[37]B. Engquist and B. Sjogreen, "The convergence rate of finite difference schemes in the presence of shocks," SIAM (Soc. Ind. Appl. Math.) J. Numer. Anal. **35**(6), 2464 (1998).
[38]E. F. Toro, *Riemann Solvers and Numerical Methods for Fluid Dynamics: A Practical Introduction* (Springer Verlag, Berlin, 2009).
[39]R. J. LeVeque, *Finite Volume Methods for Hyperbolic Problems* (Cambridge University Press, Cambridge, 2002).
[40]M. H. Carpenter, D. Gottlieb, and S. Abarbanel, "The stability of numerical boundary treatments for compact high-order finite-difference schemes," J. Comput. Phys. **108**(2), 272 (1993).
[41]D. H. Rudy and J. C. Strikwerda, "A nonreflecting outflow boundary condition for subsonic Navier-Stokes calculations," J. Comput. Phys. **36**(1), 55 (1980).
[42]K. W. Thompson, "Time-dependent boundary conditions for hyperbolic systems, II," J. Comput. Phys. **89**(2), 439 (1990).
[43]V. N. Goncharov, "Analytical model of nonlinear, single-mode, classical Rayleigh-Taylor instability at arbitrary Atwood numbers," Phys. Rev. Lett. **88**(13), 134502 (2002).
[44]S. I. Sohn, "Simple potential-flow model of Rayleigh-Taylor and Richtmyer-Meshkov instabilities for all density ratios," Phys. Rev. E **67**(2), 26301 (2003).
[45]Q. Zhang, "Analytical solutions of Layzer-type approach to unstable interfacial fluid mixing," Phys. Rev. Lett. **81**(16), 3391 (1998).
[46]D. Layzer, "On the instability of superposed fluids in a gravitational field," Astrophys. J. **122**, 1 (1955).
[47]S. I. Abarzhi, "A new type of the evolution of the bubble front in the Richtmyer-Meshkov instability," Phys. Lett. A **294**(2), 95 (2002).
[48]G. B. Whitha, *Linear and Nonlinear Waves* (Wiley, New York, 1974).
[49]G. Hazak, "Lagrangian formalism for the Rayleigh-Taylor instability," Phys. Rev. Lett. **76**(22), 4167 (1996).
[50]M. Latini, O. Schilling, and W. S. Don, "Effects of WENO flux reconstruction order and spatial resolution on reshocked two-dimensional Richtmyer–Meshkov instability," J. Comput. Phys. **221**(2), 805 (2007).
[51]S. P. D'yakov, "On the stability of shock waves," Zh. Eksp. Teor. Fiz. **27**, 288 (1954).
[52]L. D. Landau and E. M. Lifshitz, *Fluid Mechanics,Course of Theoretical Physics*, Vol. 6 (Pergamon, London, 1987).
[53]R. J. LeVeque, *Numerical Methods for Conservation Laws* (Birkhäuser, Boston, 1992).
[54]R. Samtaney and N. J. Zabusky, "Circulation deposition on shock-accelerated planar and curved density-stratified interfaces: Models and scaling laws," J. Fluid Mech. **269**(45-78), 2 (1994).
[55]K. A. Meyer and P. J. Blewett, "Numerical investigation of the stability of a shock-accelerated interface between two fluids," Phys. Fluids **15**, 753 (1972).
[56]B. J. Olson and A. W. Cook, "Rayleigh–Taylor shock waves," Phys. Fluids **19**, 128108 (2007).

Downloaded 02 Sep 2011 to 131.215.220.186. Redistribution subject to AIP license or copyright; see http://pof.aip.org/about/rights_and_permissions